www.sciencemag.org/content/347/6221/530/suppl/DC1

Supplementary Materials for

Vibrational relaxation and microsolvation of DF after F-atom reactions in polar solvents

G. T. Dunning, D. R. Glowacki,* T. J. Preston, S. J. Greaves, G. M. Greetham, I. P. Clark, M. Towrie, J. N. Harvey, A. J. Orr-Ewing*

*Corresponding author. E-mail: a.orr-ewing@bristol.ac.uk (A.J.O.-E.); drglowacki@gmail.com (D.R.G.)

Published 30 January 2015, *Science* **347**, 530 (2015)
DOI: 10.1126/science.aaa0103

This PDF file includes:

Materials and Methods

Experimental Details

Experiments were carried out using the ULTRA system at the Central Laser Facility, located at the STFC Rutherford Appleton Laboratory. The ULTRA instrumentation has been described in detail previously (*14, 28*), and a brief description is provided here. Laser pulses of duration ~50 fs were generated using an amplified Titanium: sapphire laser system operating at 10 kHz. Frequency tripling a portion of the 800-nm fundamental emission produced 267-nm ultraviolet pulses of ≤ 1 μJ per pulse for photolysis of XeF_2 in the weakly absorbing low-energy side of its UV absorption band (*29*). Probe pulses were produced either by white-light continuum (WLC) generation by focusing a further portion of the Ti:Sapphire fundamental into a rastered disc of calcium fluoride, or by difference frequency generation (DFG) using the output of an optical parametric amplifier (OPA) pumped by the Ti:Sapphire fundamental. The WLC was used as a probe pulse to follow the production and loss of XeF—F complexes, as described in a separate publication (*20*). The mid infra-red radiation obtained by the DFG process was tuned to a region centered on the DF fundamental absorption band at 2480 cm^{-1} and spanned ~500 cm^{-1}. Background signals from CaF_2 windows on the sample cell and from the solvent limited the time resolution of the experiment to 1 ps. IR light transmitted by the sample was dispersed onto a pair of 128-element mercury cadmium telluride (MCT) arrays mounted in liquid-nitrogen cooled cryostats. A portion of the IR probe light was split from the main beam before the sample and dispersed onto a separate 64-element MCT array to provide a reference spectrum. The IR beam lines were enclosed and purged with dry nitrogen to minimize losses by absorption by atmospheric water and CO_2. The UV/visible transient absorption data are reported elsewhere (*20*), and used a spectrometer comprising a grating and a 512-pixel array detector.

Further experiments to determine the vibrational relaxation rates of DF in CD_3CN or CD_2Cl_2 used an IR pump beam in place of the 267-nm pump beam described above. The IR pump beam was formed by DFG of the output of a second OPA designed to produce pulses of duration 1-2 ps, by pumping with the fundamental of a picosecond Ti:Sapphire amplifier synchronized to the femtosecond amplifier described above (*28*). These longer IR pulses had narrower bandwidths of ~12 cm^{-1}, allowing selective excitation of solvated DF molecules to v=1.

In all time-resolved spectroscopic measurements, alternate pump beam pulses were blocked by a chopper wheel to allow subtraction of pump-off spectra from pump-on spectra to isolate transient spectral features. Transient IR spectra were further processed after completion of the data acquisition by subtraction of the reference beam spectrum, and to correct for changes to the baseline induced by laser intensity fluctuations (*30*). Detector pixel to wavelength (and then wavenumber) conversion was performed using calibration spectra from samples for which multiple peak positions were accurately known from FTIR measurements.

All experiments were conducted at an ambient laboratory temperature of 20°C. Samples were prepared by dissolving 0.44 g of XeF_2 (Sigma Aldrich, 99.99%) in dry CD_3CN (Sigma Aldrich, 99.8 atom % D, anhydrous) or CD_2Cl_2 (Sigma Aldrich, 99.96 atom % D) to make 5 ml, 0.52 M solutions in a brown glass volumetric flask. The solvent was typically taken from a sealed ampoule immediately before use. XeF_2 was stored in a sealed container in a refrigerator. A peristaltic pump circulated sample solutions through PTFE tubing to and from a Harrick cell fitted with two CaF_2 windows separated by 0.2 mm by PTFE spacers. The windows were sealed to the body of the Harrick cell by Kalrez o-rings that were resistant to acetonitrile. The glassware, Harrick cell components and PTFE tubing were dried thoroughly before use, and non-polymeric components were stored in a drying oven between experiments. Circulation of the solution and rastering of the Harrick cell ensured that successive laser pulses probed fresh samples of the solution. Although the samples of XeF_2 in CD_3CN were stable over extended periods, XeF_2 solutions in chlorinated solvents decompose in Pyrex glassware (*31*). Mild warming of the XeF_2 solutions in CD_2Cl_2 caused by circulation initiated decomposition, with vigorous release of gases and evidence for reaction with the chlorinated solvent. The sealed flow system was therefore vented using a hypodermic needle inserted through a rubber septum at the top of the volumetric flask housing the sample, and the flask was held in an ice/water bath prior to, and during, transient absorption experiments. At 267 nm, d_3-acetonitrile is non-absorbing, but weak 2-photon excitation of CD_2Cl_2 can release a Cl atom that complexes to the solvent or recombines with a CD_2Cl radical (*32*). This solvent photochemistry is not considered likely to influence the experimental observations reported here, which do not probe its products.

IR-pump and IR-probe experiments used dilute solutions of DF in CD_3CN or CD_2Cl_2 that were prepared by exposure of a Harrick cell containing a static sample of XeF_2 in the chosen solvent to 267-nm radiation from a Nd:YVO_4 nanosecond laser system running at 10 kHz. Irradiation was carried out until a (weak) DF band was evident in the steady-state IR absorption spectrum of the sample.

We obtained steady-state FTIR spectra of all samples, both before and after the transient absorption experiments, and also measured FTIR spectra of the pure solvent samples in Harrick cells with 0.3-mm window spacings to identify solvent interferences with the DF bands.

Data Analysis

(I) Transient UV and visible spectra

We analysed the band intensities in transient absorption spectra obtained in the near ultra-violet and visible regions of the spectrum at time delays from 1 – 1500 ps using the procedure described in detail in reference (*20*). Two near-UV bands in the spectrum were assigned to formation of XeF (corresponding to the B-X electronic absorption centered at 345 nm) and the FXe—F solvent-caged complex (with a red-shifted absorption) (*20*), following 267-nm one-photon photoexcitation of XeF_2 solutions in CD_3CN or CD_2Cl_2. The rise of these signals is faster than the limiting time resolution of our experiments (< 1 ps). In CD_3CN solutions, XeF is stable over timescale much longer than our longest time delay, but the FXe—F complex decays with a time constant of

$\tau_F = 4.0 \pm 0.2$ ps. We attribute much of this loss to reaction of the F-atom, as discussed further below, but note that geminate recombination to XeF_2 and diffusive separation also contribute. In CD_2Cl_2 solutions, the corresponding decay time constant for the FXe—F complex is $\tau_F = 4.5 \pm 0.8$ ps, and the XeF absorption band declines with a time constant of $\tau_{XeF} = 790 \pm 80$ ps that indicates reaction with the solvent. Uncertainties quoted here all correspond to 2 standard deviations (2 SD). If the τ_F values are converted to bimolecular reaction rate coefficients (using concentrations for liquid CD_3CN and CD_2Cl_2 of 19.2 M and 15.7 M, respectively), we obtain $k = (1.30 \pm 0.05) \times 10^{10}$ M^{-1} s^{-1} for F + CD_3CN (which compares to a value of 1.6×10^{10} M^{-1} s^{-1} from reference (*33*) for F + CD_3CN in Freon-113) and $k_{bi} = (1.40 \pm 0.25) \times 10^{10}$ M^{-1} s^{-1} for F + CD_2Cl_2. The gas-phase reaction of F atoms with CH_2Cl_2 has a rate coefficient at room temperature of $(9.0 \pm 1.7) \times 10^9$ M^{-1} s^{-1} (*34*), and abstraction of an H-atom dominates.

(II) Transient IR spectra

Time-resolved IR (TRIR) absorption spectra were obtained over a range of ~500 cm^{-1} around the center of the DF fundamental band (2480 cm^{-1} in acetonitrile solution), a steady-state absorption spectrum of which is shown in figure S1. The broad IR bandwidth was necessary to capture the full DF (v=1←v=0) absorption feature, to seek evidence of vibrational hot bands, and to observe shifts in the spectrum with changing solvent environment of the DF. Both CD_3CN and CD_2Cl_2 exhibit strong solvent absorption features in this region of the IR, and although these did not mask the DF fundamental band, they obscured spectral regions where DF hot bands might be expected. Importantly, the IR bandwidth was also sufficient to span wavenumber regions free from solvent or DF absorptions, so that baseline levels corresponding to no sample absorption could be identified on both the low and high wavenumber sides of the spectral features of interest. The transient IR spectra were baseline corrected using this information prior to further analysis.

Analysis of the broad, time-dependent absorption features in TRIR spectra used the following procedure, with imposition of a number of constraints to ensure robust decomposition of the overlapping and shifting spectral bands. A Gaussian function was fitted to a late-time spectrum, to obtain the full-width at half maximum height (FWHM) and central wavenumber of the DF fundamental (v=1←v=0) band at equilibrium. The DF(v=2←v=1) band was modelled using a second Gaussian function with the same FWHM as the fundamental band, but with a center at lower wavenumber to account for anharmonicity. The center-to-center distance of the two Gaussian functions was fixed to a wavenumber interval of 140 cm^{-1} (in CD_3CN, anharmonicity constant $\omega_e x_e = 70$ cm^{-1}) or 120 cm^{-1} (in CD_2Cl_2, $\omega_e x_e = 60$ cm^{-1}) which represents an increase from the known gas-phase anharmonic separation of 91.5 cm^{-1} ($\omega_e x_e = 45.76$ cm^{-1}) (*35*). Our calculations of the vibrational frequencies of isolated and solvent-complexed DF support the increase in the anharmonicity of the vibrational motion when interacting with a solvent, and the greater effect in acetonitrile than in dichloromethane. Moreover, hydrogen bond strengths are expected to increase upon vibrational excitation of the DF, causing greater red-shifting of the v=2←v=1 band relative to the fundamental v=1←v=0 band than observed in the gas phase. The pair of bands, with fixed separation and FWHMs of the

Gaussian components, was used as a basis spectrum to fit the time-dependent IR spectra. The areas of the two Gaussian components were allowed to be independently either positive or negative to model net absorption or emission (the latter corresponding to a population inversion) between vibrational levels. Inspection of the TRIR spectra revealed that the DF (v=1←v=0) bands shifted by 90 cm^{-1} to lower wavenumber with increasing time delay, and that this shift could be fitted with an exponential time constant of 9 – 11 ps in CD_3CN and 10 – 13 ps in CD_2Cl_2. As is discussed in the main text, we attribute this shift to restructuring of the solvent environment around the reaction products. In the fits, the center wavenumbers of the two Gaussian functions were therefore allowed to shift from their initial (2570 cm^{-1} and 2430 cm^{-1}) to their equilibrium (2480 cm^{-1} and 2340 cm^{-1}) values with exponential time dependence constrained to a time constant of 9 – 11 ps. We make the simplest assumption of a constant center-to-center separation of the two functions, corresponding to a constant anharmonic spacing of the two absorption bands. The outcomes of these fits provide the time-dependent intensities of features attributed to the DF (v=2←v=1) and (v=1←v=0) transitions such as those plotted in figure 2 of the main article. These intensity data were analysed using a kinetic model that includes DF formation in a set of vibrational levels followed by relaxation to ground state DF (v=0), as described below. The model relates band intensities to time-dependent populations of DF in the different vibrational levels.

Other possible causes of the DF fundamental band shift to lower wavenumber that were considered and discounted on the basis of spectroscopic and kinetic evidence include: (i) aggregate CD_3CN-$(DF)_n$ formation (with n=2, 3), as reported in matrix isolation experiments (*24*); (ii) DF-H_2O complexes caused by trace water contamination in our solvents (*36*); (iii) DF – XeF or DF – XeF_2 complexes. The long-time DF spectra, and HF spectra we obtained for F + CH_3CN in normal acetonitrile, agree well with previously published spectra obtained at low concentrations in acetonitrile and assigned to monomeric DF or HF solutes (*21, 37, 38*), so perturbation by XeF, XeF_2 or water is not significant. Johnson and Andrews measured IR absorption spectra of CD_3CN—DF in Ar matrices at 12 K and reported DF bands centered at 2609 cm^{-1} and 2572 cm^{-1} corresponding to hydrogen-bonded DF molecules (*24*). The -100 cm^{-1} shift of the band center to 2480 cm^{-1} observed in solution is indicative of further solvation effects in d_3-acetonitrile and is consistent with the magnitude of the time-dependent shift we report here with time constant of ~10 ps. Further evidence for the several-ps time constant of this spectral red shift, and its origin in a solvation effect, is presented later.

A single set of TRIR spectra typically consisted of 40 individual spectra obtained at different time intervals from 1 – 1500 ps. As most of the changes in the spectrum occurred during the first 50 ps, the majority of the time points were selected in this early time range. Figure S2 shows examples of fits to background-corrected TRIR spectra using the procedure outlined above. Regions of the spectra masked by strong solvent absorption bands were excluded from the fitting. Other models for analysis of the spectral data were tested, but none proved as satisfactory or robust as the above method. All fitting, with the constraints described above imposed, was implemented in Origin 9 software.

At time delays longer than 50 ps, the DF bands closely resemble those obtained from steady-state FTIR measurements of solutions of DF in CD_3CN and CD_2Cl_2 (see Figure 2 of the main article). Some residual broadening of the high wavenumber side of the DF band in CD_3CN in transient spectra at delays up to 1500 ps is characteristic of a thermally shifted ground state in hydrogen-bonded solutions (*39*).

(III) Kinetic fitting of time-dependent integrated band intensities

(a) Fits to F + CD_3CN data

The model described here incorporates F-atom production, D-atom abstraction, DF formation in a range of vibrational levels, and subsequent vibrational thermalization, and was implemented to account for the time dependence of all the transient spectral features observed in the UV/visible and IR regions following XeF_2 photolysis in CD_3CN.

(i) Photolysis of XeF_2 in solution:

$$XeF_2 + UV\ (\lambda=267\ nm) \rightarrow FXe\text{—}F \qquad k_{1a} \qquad (1a)$$
$$XeF_2 + UV\ (\lambda=267\ nm) \rightarrow XeF + F \qquad k_{1b} \qquad (1b)$$

Here, FXe—F denotes an XeF radical and an F atom confined in proximity within a solvent cage (*20*), giving a pronounced red-shift to the XeF (B-X) electronic absorption band, and XeF + F denotes more completely separated photoproducts. The FXe—F is referred to as a "complex", but may consist simply of an unbound F atom and an XeF radical within the same shell of solvent molecules. Kinetic analysis of XeF_2 photolysis in CD_3CN shows that channel (1a) dominates channel (1b). We enforce prompt production of F atoms by assigning a value of $k_1 = k_{1a} + k_{1b}$ of 10 ps^{-1} because transient UV/visible absorption spectra confirm that the photodissociation of XeF_2 occurs in less than 1 ps (*20*). In their subsequent reactivity with CD_3CN, we do not distinguish between F atoms confined with a partner XeF within a solvent cage from F-atoms that escape that cage within the first ps following the photodissociation of XeF_2.

(ii) Reaction of F-atoms with the solvent CD_3CN:

$$F + CD_3CN \rightarrow DF(v=2) + CD_2CN \qquad k_2 \qquad (2)$$
$$F + CD_3CN \rightarrow DF(v=1) + CD_2CN \qquad k_3 \qquad (3)$$
$$F + CD_3CN \rightarrow DF(v=0) + CD_2CN \qquad k_4 \qquad (4)$$

The kinetics of reactions (2) – (4) are treated as *pseudo*-first order because the CD_3CN solvent is in large excess over the F atoms. The bimolecular rate coefficient for a reactive step is obtained by dividing the *pseudo*-first-order rate coefficient (k_2, k_3, k_4 or their sum k_r for the total reaction) by the concentration of the solvent (19.2 M for CD_3CN at 25°C).

For F + $CD_3CN \rightarrow$ DF + CD_2CN, inclusion of reactions to form DF(v>2) gave poorer fits to the experimental data although some higher vibrational levels are energetically accessible, so we limited DF production to v≤2. However, we cannot discount some

formation of DF(v=3) followed by sub-ps relaxation to v=2, as predicted by the MD simulations.

Figure 2 of the main article shows examples of simultaneous fits to experimental data for time-dependent band intensities for both the DF (v=2←v=1) and (v=1←v=0) transitions. The following further constraints were imposed to obtain these fits. Our analysis of XeF_2 photolysis in CD_3CN suggests that process (1a) forming XeF—F caged radical pairs dominates process (1b). Consumption of XeF—F (with time constant τ_F, see above), whether by reaction with solvent or geminate recombination, will then control the overall rate of DF production. The sum of the reaction rate coefficients must satisfy $k_2 + k_3 + k_4 = k_r = 1/\tau_F$, and this constraint was imposed for analysis of the F + CD_3CN reaction data, with the value of the total reaction rate coefficient $k_r = 1/\tau_F$ determined from transient UV/visible spectra as 0.25 ± 0.01 ps^{-1}.

Time-dependent integrated band intensities in all the TRIR spectra depend on the difference in population of the two vibrational levels connected by the transition, and on the square of the transition dipole moment. The kinetic model therefore considered population differences in DF (v=2, 1 and 0) and incorporated the ratio of the squares of transition dipole moments $(\mu_{2\text{-}1}/\mu_{1\text{-}0})^2 = 2$ expected for a harmonic oscillator.

(iii) Vibrational relaxation of the newly formed DF:

DF(v=2) → DF(v=1)	k_5	(5)
DF(v=1) → DF(v=0)	k_6	(6)

The vibrational relaxation rate coefficient k_6 was independently measured by infra-red pump and infra-red probe experiments performed with dilute solutions of DF in CD_3CN. IR excitation with a ~12 cm^{-1} bandwidth IR pump laser (1-2 ps duration) created a transient bleach in the DF (v=1←v=0) band intensity and recovery of this bleach was observed by absorption by the second, broadband IR pulse (time duration < 100 fs). Linear polarizations of the two lasers were set at the magic angle (54.7^o) to eliminate any effects of rotational reorientation dynamics in the spectra. Figure S3 shows representative data, and the derived time constant is τ_6 (=$1/k_6$) = 3.1 ± 0.6 ps in CD_3CN. By constraining k_6 in this way in the kinetic fits to reactive data, we assume that the vibrational relaxation time-constant for IR-excited DF in CD_3CN solution is the same as for DF formed by chemical reaction, which has a nearby radical co-product (*18*). We are confident of the validity of this assumption because of the strong coupling of the DF vibrational mode to the solvent, as demonstrated by the short time constants.

When the IR-pump and IR-probe experiments are repeated with the pump laser deliberately detuned by 20 cm^{-1} or more to higher wavenumber than the DF band center, the vibrational relaxation time constant determined from the bleach recovery is unchanged. However, the pump laser now excites a subset of the DF molecules in a different solvation environment from those absorbing at the band center, and depletes the ground state population of molecules in this environment. By monitoring the spectral shift in the center of the bleach feature in time-dependent spectra of the type shown in

figure S3B, the time constant for recovery of an equilibrium distribution of solvated DF molecules can be estimated. The derived time constant is ~ 6 ps, which is similar to the time constant for the red shift of the fundamental band following reactive formation of DF reported in the main paper and above.

Summary of the kinetic fitting: The only variables floated in the simultaneous fits to DF (v=2←v=1) and (v=1←v=0) band intensities were therefore a total signal amplitude (determined by the long-time intensity of the (v=1←v=0) band), k_5 (describing the v=2→v=1 relaxation in DF) and two of the three reactive rate coefficients k_2, k_3 and k_4 for production of DF(v=2, 1 and 0) (because their sum was constrained to equal $k_r = 1/\tau_F$ as discussed above). In practice, k_4 for reactive formation of DF(v=0) was consistently found to be much smaller than the other two reactive rate coefficients so was fixed to a negligible value ($k_4 = 0.001$ ps^{-1}), meaning that the fits only floated k_2 and k_5. As figure 2 demonstrates, this highly constrained model provides a satisfactory account of all the kinetic data for the F + CD_3CN reaction. Table S1 summarizes the values of rate coefficients derived from fits to five independent data sets.

The branching fractions, Γ_v=DF(v)/[DF(2)+DF(1)+DF(0)], obtained from these rate coefficients are $\Gamma_{v=2}$= 55 ± 15 %, and $\Gamma_{v=1}$ = 44 ± 15 % (with 2 SD uncertainties). In the gas phase, the F + $CH_3CN \rightarrow$ HF + CH_2CN reaction produces HF in v=3 (20%), v=2 (42%) and v=1 (38%) (*22*), and the smaller spacing of DF vibrational levels suggests the gas-phase F + $CD_3CN \rightarrow$ DF + CD_2CN will populate v≤4.

(b) Fits to F + CD_2Cl_2 data

The UV/visible transient absorption data for XeF_2 photolysis in CD_2Cl_2 indicated that the FXe—F complex decayed at a similar rate (with time constant $\tau_F = 4.5 \pm 0.8$ ps) as in CD_3CN, and we therefore assign a value of the total rate coefficient for the reaction of F atoms (or FXe—F complexes) with CD_2Cl_2, $k_r = 1/\tau_F = 0.22 \pm 0.04$ ps^{-1}. In CD_2Cl_2, pathways (1a) and (1b) are competitive in UV photolysis of XeF_2 and we assume that "free" F atoms from (1b) are consumed at the same rate as "complexed" F atoms from (1a). Fits to the time-dependent band intensities for absorption by DF(v=0) and DF(v=1), obtained from fitting the TRIR data for the F + CD_2Cl_2 reaction, using the model of equations (1) – (6), but with CD_3CN replaced by CD_2Cl_2, proved inadequate because a long-time growth was observed in the DF(v=0) fundamental band intensity. This observation is attributed to XeF reacting with the solvent, and a further step was therefore included in the kinetic model for reactions in CD_2Cl_2:

$$XeF + CD_2Cl_2 \rightarrow DF(v=0) + CDCl_2 + Xe \qquad k_7 \qquad (7)$$

This reaction also causes a slow decline in the XeF band intensity in the transient UV/visible absorption spectra, and the value of k_7 was therefore fixed to that obtained from fitting the time-dependence of the XeF (B-X) electronic band intensity, $1/k_7 = \tau_{XeF}$ =790 ± 80 ps. The vibrational relaxation rate coefficient for (6) was initially fixed to $k_6 = 0.25$ ps^{-1} on the basis of IR-pump and IR-probe data for DF in CD_2Cl_2 of the type

shown in figure S3, but fits were marginally improved by floating this parameter and it converged to a mean value (from 3 data sets) of 0.210 ± 0.074 ps^{-1}. DF(v) branching fractions were unaffected by the choice to fix or float k_6.

Solutions of XeF_2 in CD_2Cl_2 were unstable to decomposition under the conditions of our experiments (*31*), and so we were unable to obtain any further data sets of appropriate quality for analysis within the time available at the ULTRA Laser Facility.

The dynamics of F-atom reactions in CD_2Cl_2 are similar to those observed in CD_3CN. Evolution of the DF absorption bands to lower wavenumber with a time constant of 10 – 13 ps is again indicative of solvent restructuring. A greater population inversion between the product DF v=1 and v=0 levels causes the more negative-going fundamental band intensities seen in Figure 2B of the main article at early times, and v=2→1 relaxation is now faster than v=1→0. The rate of consumption of F-atoms (*20*) is also best accommodated in the fits to the kinetic model if the highest vibrational level of DF populated by the reaction is v=2, although we cannot wholly discount some production of DF(v=3). Initial relative populations of DF(v) levels are 77% in v=2 and 22% in v=1 (±11%, 2 SD), with negligible branching directly to v=0. The same reaction in the gas phase favours formation of DF(v=4 and 5). The solvent therefore quenches some, but not all, of the nascent DF vibrational excitation, either by moving the TS later along the reaction coordinate, or by coupling to the energized products as they emerge (*16*). One mechanism that might alter the location of the TS involves the reacting F atom complexing either with its geminate XeF photoproduct (*20*), or a solvent molecule.

The branching fractions, Γ_v=DF(v)/[DF(2)+DF(1)+DF(0)], obtained from these rate coefficients are $\Gamma_{v=2}$= 77 ± 11 %, and $\Gamma_{v=1}$ = 22 ± 11 % (with 2 SD uncertainties).

Computational Simulations of the F + CD_3CN reaction

Non-equilibrium dynamics simulations are notoriously sensitive to the details of the PES. In particular the MD results reported here depend sensitively on an accurate representation of two important regions of the F + CD_3CN PES, in the vicinity of: (1) the abstraction region, which determines product energy deposition; and (2) the subsequent solute-solvent complexes which may be formed upon conclusion of the abstraction reaction ($CD_2CN^{\cdots}DF$ and $CD_3CN^{\cdots}DF$) which significantly impact the relaxation dynamics of the abstraction products.

To determine an accurate set of geometries and energies in these different regions of the PES, we used the following procedure: structures for the separated reactants, the CD_2CN—DF product complex, the solvent complex CD_3CN—DF and the F---D-CD_2CN abstraction TS were optimized using density functional theory, with the M06-2X functional and the 6-311+G(d,p) basis set. Along the abstraction path, additional structures were generated by optimizing the structure of acetonitrile while holding the C-D bond length fixed at a set of values ranging from 0.8 Å to 2.8 Å, in steps of 0.1 Å. The fluorine atom was then positioned collinearly along the C-D bond direction at a set of distances. Additional structures corresponding to distorted CD_3CN—DF species were

obtained in two ways. First, this complex was re-optimized while holding the D—F distance frozen at values between 0.80 and 1.1 Å, in steps of 0.05 Å, and by varying the N-D and D-F distances while holding other coordinates fixed at those for the equilibrium CH_3CN—DF complex. Single-point energies at all these structures were computed using the CCSD(T) method with explicit treatment of electron-electron correlation using the F12-b ansatz (*40*). The cc-pVTZ basis set was used for H and C atoms, and the aug-cc-pVTZ basis for N and F. Appropriate auxiliary basis sets from the aug-cc-pVTZ family were used on all atoms. The zero-point corrected reaction energy for $F + CD_3CN \rightarrow DF + CD_2CN$ was calculated as −154.0 kJ mol^{-1}, with a forward transition state barrier of 10.5 kJ mol^{-1}, and a post-reaction CH_2CN-DF complex bound by 40.6 kJ mol^{-1}.

Running direct dynamics using the CCSD(T) methods described above would have been prohibitively expensive. It may have been possible to exploit recent advances in computational efficiency to perform DFT calculations, but the cost would have nevertheless been significant, and the results are unlikely to have yielded satisfactory statistics for interpreting the dynamics. Building on previous work, we opted for a more efficient approach: i.e., constructing a multi-state Empirical Valence Bond (EVB) model based on the CCSD(T) results. In the EVB approach, basis functions that effectively correspond to different molecular valence states are used to formulate a Hamiltonian matrix $\mathbf{H}(\mathbf{q})$ to describe the energy of a molecular system (*41*). The diagonal elements of this matrix, $V_i(\mathbf{q})$, correspond to the molecular mechanics energy of a particular valence state, using a particular connectivity scheme. The off-diagonal elements $H_{ij}(\mathbf{q})$, which we represented using two-dimensional Gaussian functions, describe how strongly different molecular configurations are coupled to one another.

To reproduce the electronic structure results described above, and to account for the fact that nascent DF formed following D abstraction from CD_3CN can complex with any of n solvent molecules included within the simulation, we required four different types of diabatic valence states. These are shown in Figure S4 for the simplest illustrative case, with $n = 2$. State 1 shows a fluorine atom nestled between two distinct solvent molecules. The other $n - 1$ solvent molecules are not reactive, but they nevertheless interact with the reacting system as it progresses along the reaction coordinate from reactants to products.[1] State 2 corresponds to the products formed following the allowed abstraction process. The nascent DF may subsequently form a post-reaction complex – with either its radical co-product, or any of the other $(n - 1)$ solvent molecules within the simulation. State 3 corresponds to deuteron transfer from DF to the nitrogen atom of its co-radical product, and state 4 corresponds to deuteron transfer from DF to the nitrogen atom of the other solvent molecule. In general, there are $(n - 1)$ replicas of state 4 (allowing DF to transfer a deuteron to every non-reactive solvent molecule in the simulation). The charge-separated states are sufficiently stabilized in solution so that the new-born and

[1] The decision to allow only one reactive deuterium is not an inherent limitation of our approach. By adding more states, it would have been possible to make it so that the fluorine could abstract any given deuterium atom, albeit at a larger computational expense. Because the emphasis in this study is on the post-TS dynamics that follow D abstraction rather than association kinetics, the error arising from this simplification is relatively minor compared to neglecting the coupling between the nascent DF and its neighboring solvent molecules.

vibrationally excited DF has the potential to transfer a D^+ to the N-atom of a nearby solvent molecule or to the CD_2CN geminate reaction product. The transient D^+ transfer occurs only during the phase of the DF vibrational cycle corresponding to an extended D-F distance.

The Hamiltonian matrix for a fluorine atom embedded in n solvent molecules thus has a dimension of $(n + 2) \times (n + 2)$, with the following structure:

$$\mathbf{H} = \begin{bmatrix} V_1 + \varepsilon_1 & H_{12} & 0 & 0 & \cdots & 0 \\ H_{12} & V_2 + \varepsilon_2 & H_{23} & H_{24} & \cdots & H_{24} \\ 0 & H_{23} & V_3 + \varepsilon_3 & 0 & \cdots & 0 \\ 0 & H_{24} & 0 & V_4 + \varepsilon_4 & \cdots & 0 \\ \vdots & \vdots & \vdots & \vdots & \ddots & 0 \\ 0 & H_{24} & 0 & 0 & 0 & V_{n+2} + \varepsilon_{n+2} \end{bmatrix} \quad (8)$$

where the diagonal elements V_1, V_2, and V_3 respectively correspond to the energies of states 1, 2, and 3 in Figure S4. Diagonal elements with indices spanning V_4 to V_{n+2} correspond to the state energies obtained following deuteron transfer from DF to each of the $(n - 1)$ solvent molecules in the simulation. To calculate the diagonal elements, we utilized the functional forms and parameters available in the Merck Molecular Mechanics force field (*42*), with some important modifications. In particular, the van der Waals parameters of the D atom in DF were changed from their default values to correspond to those of the H in H_2O. This modification was required in order to give the agreement with the CCSD(T) results in the post-reaction region of the potential (shown below). The charges on D and F were chosen to give a DF molecular dipole moment in agreement with that obtained from gas-phase DFT calculations. In addition, we tweaked the standard MMFF force-field setup to allow for the existence of (i) the F radical, (ii) sp^2 hybridized radicals of the sort that occur in the nascent CD_2CN co-product, and (iii) the CD_2CND^+ and CD_3CND^+ valence states, with charges allocated using the MMFF charge generation rules (*42*).

To obtain the results described in the paper, we modelled the reactive dynamics of an F atom embedded in 62 solvent molecules, giving a Hamiltonian matrix with dimensions of 64×64. The computational cost of these simulations is just over 64 times as large as the cost of running a typical simulation which only involves one state. The decision to utilize a 64-state matrix was determined through consideration of the number of CPU cores which we could reasonably exploit on the architectures available to us, the maximum size of the simulation required so as to quench DF without heating of the bath, and the fact that the our computational resources consist of 8-core CPU nodes. To reduce the waiting time required to complete any given simulation, we implemented a parallelized dynamics propagation strategy which works by instructing each diabatic state to calculate its energy and forces in parallel as a separate MPI process. The results for each state are then gathered together to construct the matrix elements for the Hamiltonian in Eq. (8). This matrix is subsequently diagonalized to obtain its eigenvalues and eigenvectors. Given that

force calculations are the most expensive part of classical MD propagation schemes, this parallelized propagation strategy scales nearly linearly so long as a large enough multi-core architecture is available for use during simulations. The only additional cost is that required to diagonalize the Hamiltonian matrix and calculate the Hellman-Feynman forces at each time step.

To determine the values of the Gaussian parameters used in the off-diagonal coupling elements, we implemented a Levenberg-Marquardt nonlinear least squares algorithm to fit the EVB model Hamiltonian to the CCSD(T) results. Fits to the fluorine-deuterium atom abstraction pathway, obtained by scanning over the C-D and F-D distances, are shown in Figure S5. Fits to the post-reaction CD_3CN-DF complex, obtained by scanning over the CN-DF and CND-F distances, are shown in Figure S6. The root mean squared (RMSD) average error between the fitted PES points, and the CCSD(T) points in Fig S6 is 4.4 kJ mol^{-1}, and the RMSD for Figure S7 is 8.8 kJ mol^{-1}. Rather than introduce new parameters to describe the CD_2CN-DF coupling, we assumed that it was identical to the CD_3CN-DF coupling, in line with results obtained from electronic structure theory.

Using this parallelized force field, MD simulations were performed using a locally modified, MPI-parallelized version of the CHARMM software package (*43*), with much of our own customized machinery having been described elsewhere. (*17*, *18*, *44*, *45*). All dynamics simulations began with NVT equilibration runs followed by subsequent NVE trajectories, resulting in initial conditions that were sampled using classical mechanics and the full EVB Hamiltonian. Three different types of simulation were carried out, to investigate: (1) the DF vibrational relaxation dynamics, (2) the DF microsolvation relaxation dynamics, and (3) the coupled reaction/relaxation dynamics. All simulations involving solute and solvent were carried out in a periodic box with edge lengths of 17.8 Å, in line with the room temperature experimental density of acetonitrile (0.79 g/mL at room temperature).

To investigate DF relaxation dynamics in bulk solvent, we carried out 100 separate simulations with an initial geometry wherein DF was solvated within a periodic box including 61 CD_3CN molecules, and one CD_2CN molecule. Equilibration runs of 100ps (0.5 fs timestep) with a dissipative Langevin thermostat (friction coefficient of 10 ps^{-1}, and a heat bath of 300K) were used to generate an ensemble of initial coordinates and velocities. These coordinates and velocities were used as starting points for subsequent NVE trajectories, with a duration of 10ps (0.1 fs timestep). Before launching the NVE trajectories, the velocity of the D atom in DF was given a non-equilibrium 'kick' of $\approx$146 kJ mol^{-1} in the direction of its bonded fluorine neighbor using a local-mode approach of the sort described previously (*46*). This quantity of energy essentially corresponds to the limit that all of the excess reaction energy is deposited in the product DF.

For the reaction dynamics, we initialized the simulations with an F radical embedded in 62 CD_3CN solvent molecules, and carried out 200 separate reactive trajectory simulations using equilibration runs of 100ps (0.5 fs timestep) with a dissipative Langevin thermostat (friction coefficient of 10 ps^{-1}, and a heat bath of 300K). The ensemble of initial

coordinates and velocities generated in these trajectories was used to launch subsequent NVE trajectories, with a duration of 20ps (0.1 fs timestep). To guarantee that every one of the NVE trajectories resulted in a reaction and thereby improve the statistics of the analyses carried out below, we exploited the recently developed BXD class of algorithms, which simultaneously accelerates reactive sampling and preserves meaningful non-equilibrium relaxation statistics in the wake of reaction (*47, 48*). During the equilibration runs, we specified BXD constraints to ensure that the distance between the fluorine radical and the reactive D-atom had a lower bound of 1.5 Å and an upper bound of 1.8 Å, which is well on the reactant side of the abstraction TS. In the NVE runs, the lower bound BXD constraint was relaxed, accelerating the rate of transition state passage and resulting in every trajectory undergoing an abstraction event, usually within 0.5 ps of the first timestep.

To investigate the microsolvation dynamics of DF following abstraction, we carried out reactive dynamics simulations identical to those described above, with one important difference: the vibrational excitation of the nascent DF was damped immediately following the abstraction event (i.e., at the moment of first passage through the DF equilibrium geometry), modifying the D velocity in the DF vibrational frame so as to remove all non-thermal vibrational excitation. This provided a set of trajectories where the initial coordinates of the solute and solvent are sampled from the distribution that follows in the immediate wake of abstraction, but with a thermal distribution of velocities for the CD_3CN solvent and DF solute. The utility of these 'damped trajectories' is that they provide a baseline against which to compare any dynamics which arises as a consequence of DF vibrational excitation. Any time-dependence observed for DF in the damped trajectories may be assigned to relaxation of DF within the non-equilibrium solvent environment in which it finds itself immediately following the abstraction event.

Upon completion, all of the trajectories described above were examined to ensure that they satisfied energy conservation to better than 1% of the total kinetic and potential energy. It is not uncommon that dynamics simulations carried out utilizing multi-state EVB methods fail to conserve energy, owing to an incomplete basis set of valence states in Eq. (8). *(49)*. Because our simulations included all possible couplings for a specified valence state (i.e., the Hamiltonian matrix included the interaction of DF with every possible solvent molecule), they were not subject to this source of error. Rather, any errors in energy conservation arose because of the large amount of energy ($\approx$146 kJ mol^{-1}) initially localized in the DF stretching motion. The small number of trajectories with poor energy conservation were excluded from the analyses described in the paper.

Time dependent energies of DF were determined using the strategy outlined in previous work, by projecting the coordinates and velocities into the normal-mode Eckart frame of equilibrium DF (*17, 18*). Plots of energy vs. time were then constructed by averaging over all the trajectories which were run. Quantization of the energy content of the nascent DF was obtained through a simple rectangular binning technique, wherein the total energy in the DF stretch mode (kinetic + potential) was analysed, and the result then assigned to bins whose width corresponds to a single quantum of vibrational energy (with

a harmonic spacing of 3000 cm^{-1}). The spectra reported in the paper were obtained from the well-known relationship that links a power spectrum to the Fourier transform of some dynamical observable $C(t)$:

$$I(\omega) = \frac{1}{2\pi}\int_{-\infty}^{\infty} C(t)\, exp(-i\omega t)dt \quad (9)$$

recast in an alternative form that permits one to utilize faster Fourier algorithms to obtain power spectra from dynamical observables which have a finite time duration, $2T$:

$$I(\omega) = \frac{1}{2\pi}\lim_{T\to\infty}\frac{1}{2T}\left\langle\left|\int_0^{2T} C(t)\, exp(-i\omega t)dt\right|^2\right\rangle \quad (10)$$

Here, the angled brackets indicate an average over trajectories launched with different sets of initial conditions. In this work, $C(t)$ was taken to be the velocity autocorrelation function, i.e., $\langle v(0)\cdot v(t)\rangle$ where v is a vector containing all the velocities of a relevant set of atoms. The spectral results reported herein utilize a sampling frequency of 1 fs (i.e., sampling every 10 time steps), which allow us to detect periodic motion with frequencies of ~16,000 cm^{-1} or less according to the Nyquist theorem. The spectral resolution of Eq. (10) depends on how large a time window, $2T$, is spanned by the correlation function. All time-dependent spectra were calculated from correlation functions with a length of 1.024 ps (i.e., $2T$ = 1024 fs). Figure S7 shows the spectrum calculated from a single long equilibrium trajectory. The spectrum shows solvent bands between 2000 and 2320 cm^{-1}, with the DF vibrational peak centred at 2540 cm^{-1} (a solvachromatic shift of 460 cm^{-1} compared to the classical gas-phase frequency of 3000 cm^{-1} predicted by the force field utilized within our simulations). Experimentally, the DF band is centered at 2480 cm^{-1} in CD_3CN solution and the gas-phase DF fundamental vibrational band origin is centered at 2907 cm^{-1}.

A number of features arise from the simulations that support the experimental analysis and provide further mechanistic insights. The DF forms with an average vibrational energy of 100 kJ mol^{-1} that corresponds to a vibrational quantum number between 2 and 3. Two timescales for loss of this excess energy (1.0 and 11.3 ps) are broadly consistent with the experimental observations for relaxation of vibrationally hot DF from the exothermic reaction. The simulated DF absorption spectra show a fast shift to lower wavenumber at early times, with a time constant of 0.35 ps, and a slower shift to higher wavenumber with time constant 10.2 ps. The latter shift is consistent with changes to absorption bands associated with vibrational relaxation of initially D-F stretch excited reaction products. The fast shift to lower wavenumber is attributed to initial solvation via hydrogen-bonding with solvent of the newly formed DF, and is comparable in time scale to previous reports of fast solvation of photo-excited states by acetonitrile achieved by partial reorientation of the molecules in a solvent shell (*23, 50, 51*). Observation of individual trajectories demonstrates that the DF reorients to a hydrogen-bonding configuration with an acetonitrile molecule within a few hundred fs and exchanges solvent partner on a much longer timescale of perhaps 10 ps on average. The radial distribution function corresponding to the distance between the D atom and an N atom in acetonitrile evolves with a time constant of 1.2 ps. As discussed in the main text, the

non-equilibrium MD simulations also reveal a spectral feature to the blue of the primary DF band center (see, e.g., Figure 4 panels A1-A3) whose relaxation is incomplete on the 20-ps timescale of our MD runs. This feature is linked to DF molecules with a distribution of solvation environments that are not fully relaxed, in which solvent hydrogen bonding is not fully established. This peak eventually red shifts as the DF microsolvation environment approaches equilibrium, in qualitative agreement with experimental observations.

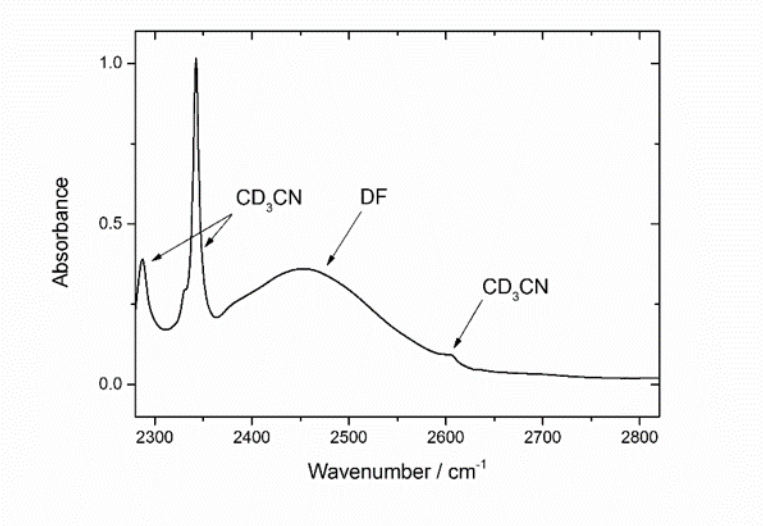

Fig. S1.

Steady-state FTIR spectrum of DF in CD_3CN. A spectrum of pure CD_3CN has been subtracted to reveal the solute band, and the sharp features are the result of imperfect subtraction of strong solvent bands.

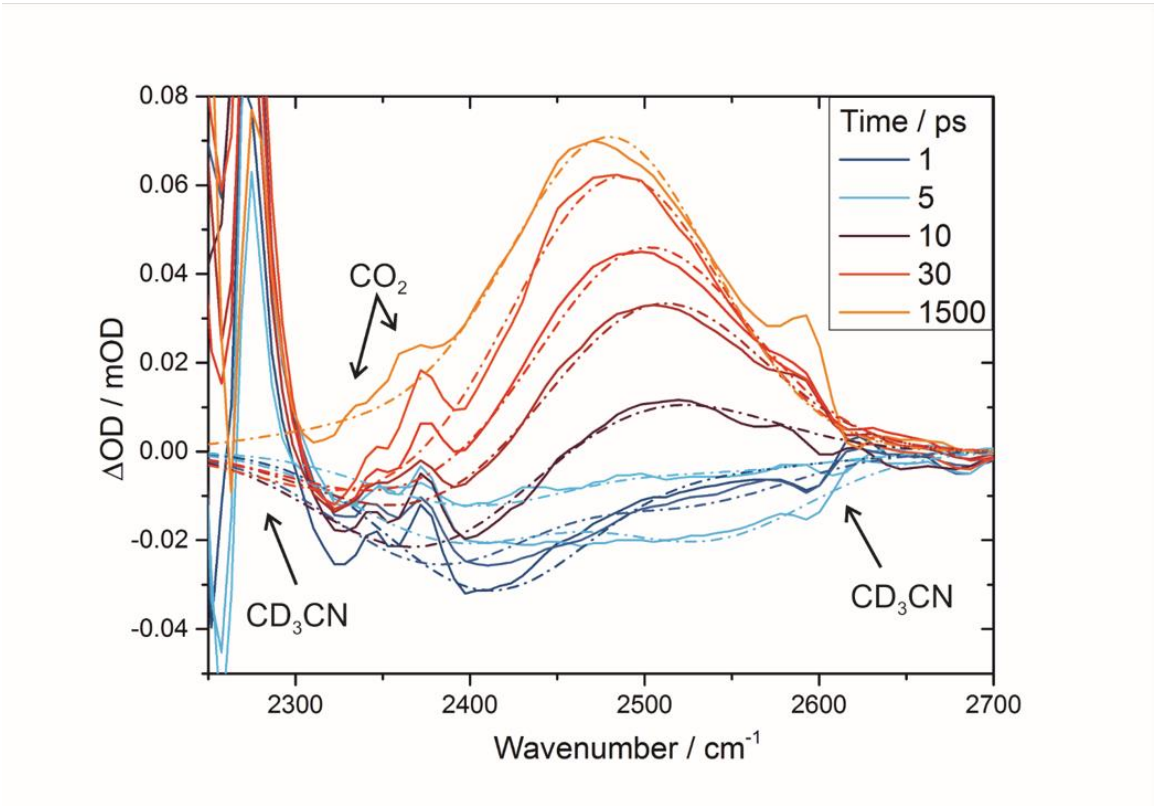

Fig. S2

Experimental (solid lines) and fitted (dot-dash lines) spectra of DF from the F + CD_3CN reaction at representative time delays after initiation of reaction. The inset key shows the color coding used for the time delays. The fits were performed using the method described in the text. Interfering absorptions from CO_2 (in the IR laser beam path) and CD_3CN are indicated.

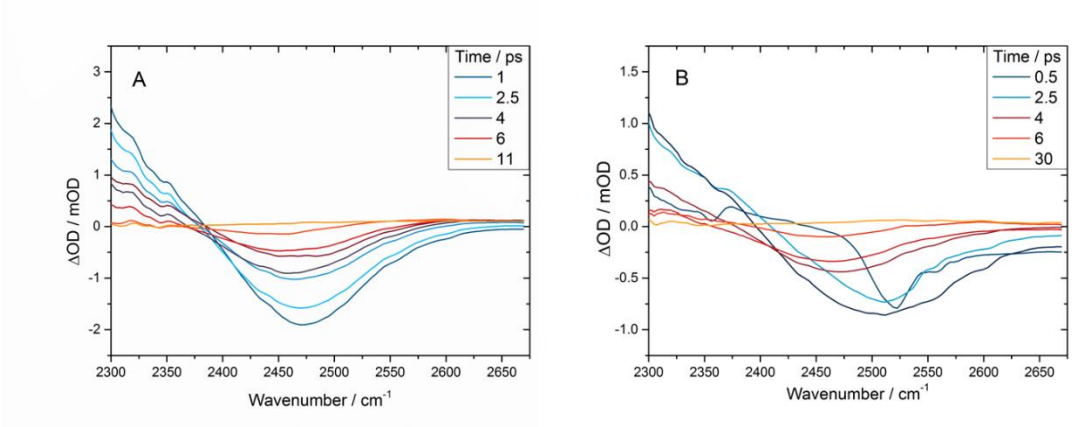

Fig. S3

IR pump and IR probe spectra for DF in CD_3CN, with (A) excitation of DF at the center of the fundamental band; (B) excitation 20 cm^{-1} higher in wavenumber than the fundamental band center. Spectra are shown only for a selection of the full set of experimental time delays. The time constant for recovery of the DF(v=0→1) band bleach obtained from the data in (A) is 3.1 ± 0.6 ps. In panel (B), the narrow bandwidth IR pump pulse selects a subset of DF molecules from the inhomogeneously broadened spectral band, and the evolution of the bleach feature center and width with time indicates spectral diffusion as the equilibrium distribution of solvated environments recovers.

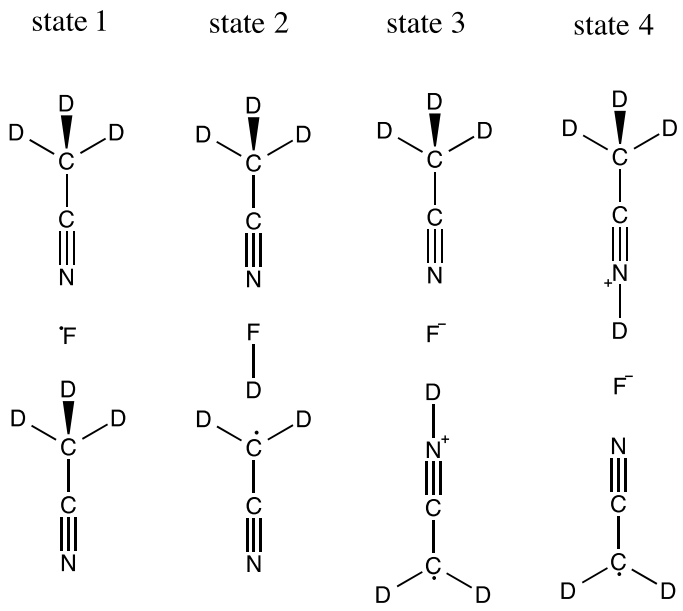

Fig. S4

Schematic diagram of the diabatic states used in our model. For simplicity, we have shown the states that arise for a Fluorine radical embedded in a solvent bath composed of only two CD_3CN solvent molecules. For the simulations detailed in the text, F was embedded in $n = 62$ solvent molecules.

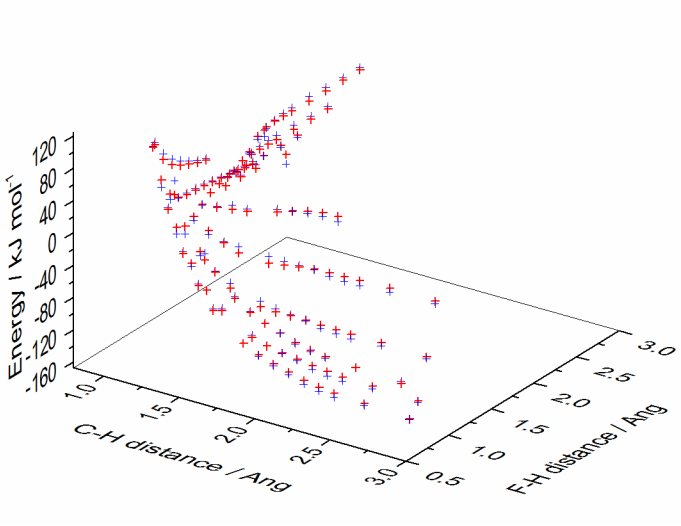

Fig. S5

Comparison between the CCSD(T) energies (blue) and the optimized MS-EVB model (red) for geometries sampled along the abstraction reaction path.

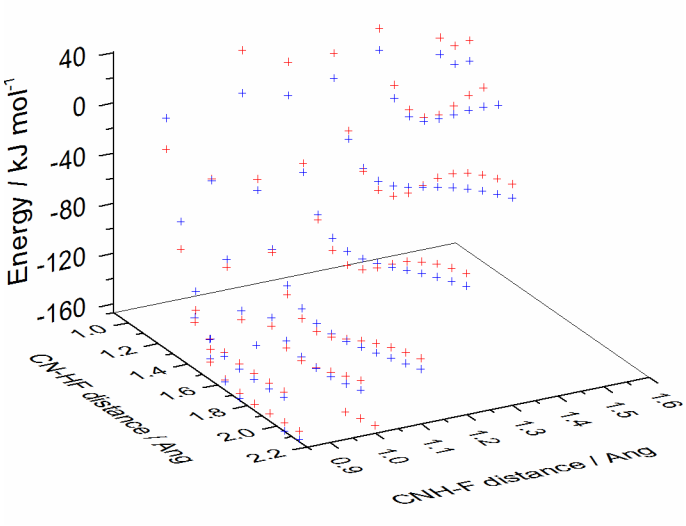

Fig. S6

Comparison between the CCSD(T) energies (blue) and the optimized MS-EVB model (red) for geometries sampled in the vicinity of the CD_3CN-DF complex.

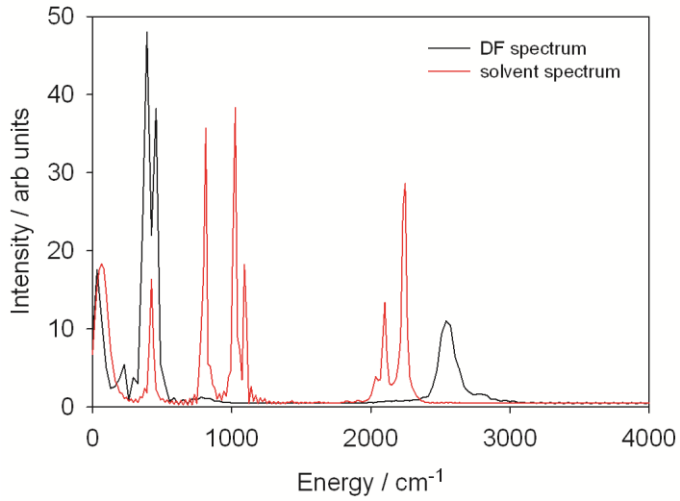

Fig. S7

Equilibrium spectra of DF embedded in CD_3CN solvent (black), and neat CD_3CN solvent (red). Note that the DF spectral data has been arbitrarily scaled to clarify its spectral features; otherwise it is dwarfed by the relative magnitudes of the solvent peaks. The DF spectral peak is well fitted with a single Gaussian function centered at 2540 cm^{-1}.

Table S1.

Fit outcomes for the kinetic model applied to data for the $F + CD_3CN \rightarrow DF + CD_2CN$ reaction. Rate coefficients are defined in the text.

	Rate coefficients in CD_3CN / ps^{-1}					
Dataset	k_1 *	k_2	k_3	k_4 †	k_5	k_6 ‡
1	10	0.144 ± 0.005	0.105 ± 0.005	0.001	0.121 ± 0.008	0.320
2	10	0.173 ± 0.015	0.076 ± 0.015	0.001	0.148 ± 0.022	0.320
3	10	0.147 ± 0.007	0.102 ± 0.007	0.001	0.113 ± 0.011	0.320
4	10	0.155 ± 0.011	0.094 ± 0.011	0.001	0.156 ± 0.019	0.320
5	10	0.121 ± 0.005	0.128 ± 0.005	0.001	0.105 ± 0.016	0.320
Mean § ± 2 SD		0.138 ± 0.038	0.111 ± 0.038		0.122 ± 0.044	

Errors specified for each dataset are the 5-95% confidence range from fits.

* Fixed from evidence from transient UV/visible spectra.

† Fixed in fits

‡ Fixed from IR-pump and IR-probe experiments

§ Variance weighted means

Table S2.

Fit outcomes for the kinetic model applied to data for the F + CD_2Cl_2 → DF + $CDCl_2$ reaction. Rate coefficients are defined in the text. Values of k_7 were obtained from transient UV/visible absorption measurements, and were not floated in the fits.

	Rate coefficients in CD_2Cl_2 / ps^{-1}					
Dataset	k_1 *	k_2	k_3	k_4 †	k_5	k_6
1	10	0.171 ± 0.007	0.048 ± 0.007	0.001	0.251 ± 0.019	0.206 ± 0.012
2	10	0.167 ± 0.012	0.052 ± 0.012	0.001	0.254 ± 0.036	0.233 ± 0.026
3	10	0.189 ± 0.040	0.030 ± 0.040	0.001	0.327 ± 0.075	0.159 ± 0.075
Mean § ± 2 SD		0.170 ± 0.024	0.049 ± 0.024		0.255 ± 0.086	0.210 ± 0.074

Errors specified for each dataset are the 5-95% confidence range from fits.

* Fixed from evidence from transient UV/visible spectra.

† Fixed in fits

§ Variance weighted means

References

1. R. D. Levine, *Molecular Reaction Dynamics* (Cambridge Univ. Press, Cambridge, 2005).

2. D. M. Neumark, A. M. Wodtke, G. N. Robinson, C. C. Hayden, Y. T. Lee, Molecular-beam studies of the F+H_2 Reaction. *J. Chem. Phys.* **82**, 3045–3066 (1985). doi:10.1063/1.448254

3. W. Dong, C. Xiao, T. Wang, D. Dai, X. Yang, D. H. Zhang, Transition-state spectroscopy of partial wave resonances in the F + HD reaction. *Science* **327**, 1501–1502 (2010). Medline doi:10.1126/science.1185694

4. D. E. Manolopoulos, K. Stark, H. J. Werner, D. W. Arnold, S. E. Bradforth, D. M. Neumark, The transition state of the F + H_2 reaction. *Science* **262**, 1852–1855 (1993). Medline doi:10.1126/science.262.5141.1852

5. M. Tizniti, S. D. Le Picard, F. Lique, C. Berteloite, A. Canosa, M. H. Alexander, I. R. Sims, The rate of the F + H_2 reaction at very low temperatures. *Nat. Chem.* **6**, 141–145 (2014). Medline doi:10.1038/nchem.1835

6. M. Qiu, Z. Ren, L. Che, D. Dai, S. A. Harich, X. Wang, X. Yang, C. Xu, D. Xie, M. Gustafsson, R. T. Skodje, Z. Sun, D. H. Zhang, Observation of Feshbach resonances in the F+H_2 → HF+H reaction. *Science* **311**, 1440–1443 (2006). Medline doi:10.1126/science.1123452

7. T. Wang, J. Chen, T. Yang, C. Xiao, Z. Sun, L. Huang, D. Dai, X. Yang, D. H. Zhang, Dynamical resonances accessible only by reagent vibrational excitation in the F + HD->HF + D reaction. *Science* **342**, 1499–1502 (2013). Medline doi:10.1126/science.1246546

8. R. Otto, J. Ma, A. W. Ray, J. S. Daluz, J. Li, H. Guo, R. E. Continetti, Imaging dynamics on the F + H_2O → HF + OH potential energy surfaces from wells to barriers. *Science* **343**, 396–399 (2014). Medline doi:10.1126/science.1247424

9. L. Che, Z. Ren, X. Wang, W. Dong, D. Dai, X. Wang, D. H. Zhang, X. Yang, L. Sheng, G. Li, H. J. Werner, F. Lique, M. H. Alexander, Breakdown of the Born-Oppenheimer approximation in the F+*o*-D_2 → DF+D reaction. *Science* **317**, 1061–1064 (2007). Medline doi:10.1126/science.1144984

10. J. J. Lin, J. Zhou, W. Shiu, K. Liu, State-specific correlation of coincident product pairs in the F + CD_4 reaction. *Science* **300**, 966–969 (2003). Medline doi:10.1126/science.1083672

11. M. A. Wickramaaratchi, D. W. Setser, H. Hildebrandt, B. Körbitzer, H. Heydtmann, Evaluation of HF product distributions deduced from infrared chemiluminescence. 2. F-atom reactions. *Chem. Phys.* **94**, 109–129 (1985). doi:10.1016/0301-0104(85)85070-9

12. J. C. Polanyi, Concepts in reaction dynamics. *Acc. Chem. Res.* **5**, 161–168 (1972). doi:10.1021/ar50053a001

13. A. M. Zolot, P. J. Dagdigian, D. J. Nesbitt, Quantum-state resolved reactive scattering at the gas-liquid interface: F+squalane ($C_{30}H_{62}$) dynamics via high-resolution infrared

absorption of nascent HF(v,J). *J. Chem. Phys.* **129**, 194705 (2008). Medline doi:10.1063/1.2973630

14. S. J. Greaves, R. A. Rose, T. A. A. Oliver, D. R. Glowacki, M. N. R. Ashfold, J. N. Harvey, I. P. Clark, G. M. Greetham, A. W. Parker, M. Towrie, A. J. Orr-Ewing, Vibrationally quantum-state-specific reaction dynamics of H atom abstraction by CN radical in solution. *Science* **331**, 1423–1426 (2011). Medline doi:10.1126/science.1197796

15. R. A. Rose, S. J. Greaves, T. A. A. Oliver, I. P. Clark, G. M. Greetham, A. W. Parker, M. Towrie, A. J. Orr-Ewing, Vibrationally quantum-state-specific dynamics of the reactions of CN radicals with organic molecules in solution. *J. Chem. Phys.* **134**, 244503 (2011). Medline doi:10.1063/1.3603966

16. A. J. Orr-Ewing, Perspective: Bimolecular chemical reaction dynamics in liquids. *J. Chem. Phys.* **140**, 090901 (2014). Medline doi:10.1063/1.4866761

17. D. R. Glowacki, A. J. Orr-Ewing, J. N. Harvey, Product energy deposition of CN + alkane H abstraction reactions in gas and solution phases. *J. Chem. Phys.* **134**, 214508–214511 (2011). Medline doi:10.1063/1.3595259

18. D. R. Glowacki, R. A. Rose, S. J. Greaves, A. J. Orr-Ewing, J. N. Harvey, Ultrafast energy flow in the wake of solution-phase bimolecular reactions. *Nat. Chem.* **3**, 850–855 (2011). Medline doi:10.1038/nchem.1154

19. G. T. Dunning, T. J. Preston, A. J. Orr-Ewing, S. J. Greaves, G. M. Greetham, I. P. Clark, M. Towrie, Dynamics of photodissociation of XeF_2 in organic solvents. *Phys. Chem. Chem. Phys.* **16**, 16095–16102 (2014). Medline doi:10.1039/C4CP01854K

20. Materials and methods are available as supporting material on *Science* Online.

21. R. M. Adams, J. J. Katz, Infrared spectral studies of hydrogen bonding phenomena in solutions containing hydrogen fluoride. *J. Mol. Spectrosc.* **1**, 306–332 (1957). doi:10.1016/0022-2852(57)90032-2

22. K. Dehe, H. Heydtmann, HF infrared emission from the reactions of atomic fluorine with methylcyanide, methylisocyanide, dimethylsulfide and dimethyldisulfide. *Chem. Phys. Lett.* **262**, 683–688 (1996). doi:10.1016/S0009-2614(96)01148-7

23. B. Bagchi, B. Jana, Solvation dynamics in dipolar liquids. *Chem. Soc. Rev.* **39**, 1936–1954 (2010). Medline doi:10.1039/b902048a

24. G. L. Johnson, L. Andrews, Infrared spectra of hydrogen-bonded complexes between methyl cyanide and hydrogen fluoride in solid argon at 12 K. *J. Phys. Chem.* **87**, 1852–1859 (1983). doi:10.1021/j100234a006

25. R. Rey, K. B. Møller, J. T. Hynes, Hydrogen bond dynamics in water and ultrafast infrared spectroscopy. *J. Phys. Chem. A* **106**, 11993–11996 (2002). doi:10.1021/jp026419o

26. W. L. Jorgensen, J. M. Briggs, Monte Carlo simulations of liquid acetonitrile with a three-site model. *Mol. Phys.* **63**, 547–558 (1988). doi:10.1080/00268978800100371

27. C. R. Nicoleti, V. G. Marini, L. M. Zimmermann, V. G. Machado, Anionic chromogenic chemosensors highly selective for fluoride or cyanide based on 4-(4-

nitrobenzylideneamine)phenol. *J. Braz. Chem. Soc.* **23**, 1488–1500 (2012). doi:10.1590/S0103-50532012005000007

28. G. M. Greetham, P. Burgos, Q. Cao, I. P. Clark, P. S. Codd, R. C. Farrow, M. W. George, M. Kogimtzis, P. Matousek, A. W. Parker, M. R. Pollard, D. A. Robinson, Z.-J. Xin, M. Towrie, ULTRA: A unique instrument for time-resolved spectroscopy. *Appl. Spectrosc.* **64**, 1311–1319 (2010). Medline doi:10.1366/000370210793561673

29. G. Black, R. L. Sharpless, D. C. Lorents, D. L. Huestis, R. A. Gutcheck, T. D. Bonifield, D. A. Helms, G. K. Walters, XeF_2 photo-dissociation studies. 1. Quantum yields and kinetics of XeF(B) and XeF(C). *J. Chem. Phys.* **75**, 4840–4846 (1981). doi:10.1063/1.441920

30. M. P. Grubb, A. J. Orr-Ewing, M. N. R. Ashfold, KOALA: A program for the processing and decomposition of transient spectra. *Rev. Sci. Instrum.* **85**, 064104 (2014). Medline doi:10.1063/1.4884516

31. M. M. Shaw, R. G. Smith, C. A. Ramsden, F-19 NMR and UV studies of xenon difluoride solution-vessel stability and its relevance to the fluorination of organic substrates. *ARKIVOC* **2011**, 221–228 (2011). doi:10.3998/ark.5550190.0012.a18

32. F. Abou-Chahine, T. J. Preston, G. T. Dunning, A. J. Orr-Ewing, G. M. Greetham, I. P. Clark, M. Towrie, S. A. Reid, Photoisomerization and photoinduced reactions in liquid CCl_4 and $CHCl_3$. *J. Phys. Chem. A* **117**, 13388–13398 (2013). Medline doi:10.1021/jp406687x

33. G. Bucher, J. C. Scaiano, Absolute rate constants for atomic fluorine in solution - characterization of reaction intermediates in the laser flash-photolysis of xenon difluoride. *J. Am. Chem. Soc.* **116**, 10076–10079 (1994). doi:10.1021/ja00101a028

34. G. LeBras, N. I. Butkovskaya, I. I. Morozov, V. L. Talrose, Reaction of F-atoms with dichloromethane by modulated molecular-beam mass-spectrometry. *Chem. Phys.* **50**, 63–69 (1980). doi:10.1016/0301-0104(80)87025-X

35. NIST Webbook, *National Institute of Standards and Technology*, P. J. Linstrom, W. G. Mallard, Eds. (NIST, Gaithersburg, MD, 2011).

36. L. Andrews, G. L. Johnson, FTIR spectra of water hydrogen-fluoride complexes in solid argon: Evidence for inversion doubling in the HF librational modes of H_2O-HF. *J. Chem. Phys.* **79**, 3670–3677 (1983). doi:10.1063/1.446286

37. N. I. Sushko, V. F. Sukhoverkhov, E. G. Tarakanova, G. V. Yukhnevich, The IR spectra of solutions of hydrogen fluoride in $(CH_3)_2NCHO$, $(CH_3)_2CO$, and CH_3CN with a molar ratio of the components of 0: 1-10: 1. *J. Opt. Technol.* **73**, 515–518 (2006). doi:10.1364/JOT.73.000515

38. G. V. Yukhnevich, E. G. Tarakanova, IR spectroscopic analysis of the composition of heterocomplexes formed in a binary system. *Opt. Spectrosc.* **101**, 708–715 (2006). doi:10.1134/S0030400X06110099

39. R. A. Nicodemus, S. A. Corcelli, J. L. Skinner, A. Tokmakoff, Collective hydrogen bond reorganization in water studied with temperature-dependent ultrafast infrared spectroscopy. *J. Phys. Chem. B* **115**, 5604–5616 (2011). Medline doi:10.1021/jp111434u

40. H. J. Werner, G. Knizia, F. R. Manby, Explicitly correlated coupled cluster methods with pair-specific geminals. *Mol. Phys.* **109**, 407–417 (2011). doi:10.1080/00268976.2010.526641

41. A. Warshel, R. M. Weiss, An empirical valence bond approach for comparing reactions in solutions and in enzymes. *J. Am. Chem. Soc.* **102**, 6218–6226 (1980). doi:10.1021/ja00540a008

42. T. A. Halgren, Merck molecular force field. 1. Basis, form, scope, parameterization, and performance of MMFF94. *J. Comput. Chem.* **17**, 490–519 (1996). doi:10.1002/(SICI)1096-987X(199604)17:5/6<490::AID-JCC1>3.0.CO;2-P

43. B. R. Brooks, C. L. Brooks 3rd, A. D. Mackerell Jr., L. Nilsson, R. J. Petrella, B. Roux, Y. Won, G. Archontis, C. Bartels, S. Boresch, A. Caflisch, L. Caves, Q. Cui, A. R. Dinner, M. Feig, S. Fischer, J. Gao, M. Hodoscek, W. Im, K. Kuczera, T. Lazaridis, J. Ma, V. Ovchinnikov, E. Paci, R. W. Pastor, C. B. Post, J. Z. Pu, M. Schaefer, B. Tidor, R. M. Venable, H. L. Woodcock, X. Wu, W. Yang, D. M. York, M. Karplus, CHARMM: The biomolecular simulation program. *J. Comput. Chem.* **30**, 1545–1614 (2009). Medline doi:10.1002/jcc.21287

44. D. R. Glowacki, A. J. Orr-Ewing, J. N. Harvey, A parallel multistate framework for atomistic non-equilibrium reaction dynamics of solutes in strongly interacting organic solvents. http://arxiv.org/abs/1412.4180 (2014).

45. R. A. Rose, S. J. Greaves, F. Abou-Chahine, D. R. Glowacki, T. A. A. Oliver, M. N. R. Ashfold, I. P. Clark, G. M. Greetham, M. Towrie, A. J. Orr-Ewing, Reaction dynamics of CN radicals with tetrahydrofuran in liquid solutions. *Phys. Chem. Chem. Phys.* **14**, 10424–10437 (2012). Medline doi:10.1039/c2cp40158d

46. D. R. Glowacki, S. K. Reed, M. J. Pilling, D. V. Shalashilin, E. Martínez-Núñez, Classical, quantum and statistical simulations of vibrationally excited $HOSO_2$: IVR, dissociation, and implications for OH + SO_2 kinetics at high pressures. *Phys. Chem. Chem. Phys.* **11**, 963–974 (2009). Medline doi:10.1039/b816108a

47. D. R. Glowacki, E. Paci, D. V. Shalashilin, Boxed molecular dynamics: A simple and general technique for accelerating rare event kinetics and mapping free energy in large molecular systems. *J. Phys. Chem. B* **113**, 16603–16611 (2009). Medline doi:10.1021/jp9074898

48. D. R. Glowacki, E. Paci, D. V. Shalashilin, Boxed molecular dynamics: Decorrelation time scales and the kinetic master equation. *J. Chem. Theory Comput.* **7**, 1244–1252 (2011). doi:10.1021/ct200011e

49. G. A. Voth, Computer simulation of proton solvation and transport in aqueous and biomolecular systems. *Acc. Chem. Res.* **39**, 143–150 (2006). Medline doi:10.1021/ar0402098

50. M. L. Horng, J. A. Gardecki, A. Papazyan, M. Maroncelli, Subpicosecond Measurements of polar solvation dynamics: Coumarin-153 revisited. *J. Phys. Chem.* **99**, 17311–17337 (1995). doi:10.1021/j100048a004

51. S. J. Rosenthal, X. L. Xie, M. Du, G. R. Fleming, Femtosecond solvation dynamics in acetonitrile: Observation of the inertial contribution to the solvent response. *J. Chem. Phys.* **95**, 4715–4718 (1991). doi:10.1063/1.461742